Wind and Structures, *Vol. 24, No. 3 (2017) 223-247*
DOI: https://doi.org/10.12989/was.2017.24.3.223

Mesh size refining for a simulation of flow around a generic train model

Izuan Amin Ishak*, Mohamed Sukri Mat Ali[a] and Sheikh Ahmad Zaki Shaikh Salim[b]

Wind Engineering, Malaysia-Japan International Institute of Technology, UTM Kuala Lumpur, Malaysia

(Received May 18, 2016, Revised December 1, 2016, Accepted December 3, 2016)

Abstract. By using numerical simulation, vast and detailed information and observation of the physics of flow over a train model can be obtained. However, the accuracy of the numerical results is questionable as it is affected by grid convergence error. This paper describes a systematic method of computational grid refinement for the Unsteady Reynolds Navier-Stokes (URANS) of flow around a generic model of trains using the OpenFOAM software. The sensitivity of the computed flow field on different mesh resolutions is investigated in this paper. This involves solutions on three different grid refinements, namely fine, medium, and coarse grids to investigate the effect of grid dependency. The level of grid independence is evaluated using a form of Richardson extrapolation and Grid Convergence Index (GCI). This is done by comparing the GCI results of various parameters between different levels of mesh resolutions. In this study, monotonic convergence criteria were achieved, indicating that the grid convergence error was progressively reduced. The fine grid resolution's GCI value was less than 1%. The results from a simulation of the finest grid resolution, which includes pressure coefficient, drag coefficient and flow visualization, are presented and compared to previous available data.

Keywords: Grid Convergence Index; generic train; CFD simulation; OpenFOAM; flow physics

1. Introduction

The study of flow around a train model has been the subject of intense research (Hemida and Krajnovic (2009), Krajnovic *et al.* (2012), Biadgo *et al.* (2014), Rezvani *et al.* (2014)). The rapid development of high-speed trains (HST) especially in Europe, Japan and other countries has gained widespread attention. Aggressive improvement in HST technology expansion in the last three decades shows a trend toward a faster and more energy efficient model. This shapes the resurgent interest among travelers. However, awareness of safety factors has increased considerably, especially in the subject of crosswind stability. Thus, details of the flow fields surrounding a train and its aerodynamic characteristics have become more critical in terms of operational safety.

There are two main factors that may lead to inconsistencies of simulation results in the context of investigating the flow field around a train using numerical analysis. First is due to the different

*Corresponding author, Ph.D. Student, E-mail: izuan.amin@gmail.com
[a] Senior Lecturer, E-mail: sukri.kl@utm.my
[b] Senior Lecturer, E-mail: sheikh.kl@utm.my

http://www.techno-press.org/?journal=was&subpage=8 ISSN: 1226-6116 (Print), 1598-6225 (Online)

shapes of trains that are modelled. There are complex train models with additional structures such as a front spoiler, bogies and pantographs, and there are others that define the structure much more simply. Chiu and Squire (1992) and Chiu (1995), found that flow over a real train involves various complexities which are challenging to be modelled. The study by Hemida and Krajnovic (2009) used a train model without underbody complexities or inter-carriage gaps between coaches, and produced good results comparable to other studies. A study by Khier *et al.* (2000) concluded that a reduction in length will not change the important physical features of the flow since the downstream flow characteristics of a certain distance from the nose of the train (less than one coach length) are comparatively constant. In addition, the execution of numerical simulation for a complete train length requires more advanced computational resources. Thus, this study used a simplified and shortened form of the train model in order to reduce computational cost as well as to optimize simulation time.

Secondly, differences in the construction of the mesh resolutions might contribute to the deviation of simulation results. For instance, Hemida and Krajnovic (2009) constructed a computational grid containing two mesh resolutions to investigate the flow over a simplified ICE2 train subjected to side wind forces. Even though both of the grid resolutions generally gave similar results, the coarse mesh of 6 million total grid cells did not accurately predict the minimum pressure relative to the finer mesh of 12 million total grid cells. The resolution of the coarse mesh was not sufficient to get results that agree well with the experimental data at a location far from the nose of the train especially on the bottom and top side faces. In addition, Hemida and Baker (2010) studied the effects of three grid resolutions i.e., coarse mesh (3 million cells), medium mesh (5 million cells) and fine mesh (7 million cells) on the flow around a freight wagon subjected to crosswind. They found that the medium and fine meshes produced similar surface pressure distributions on all faces of the container, while the coarse grid produced lower surface pressure distributions on the top, lee and bottom faces. It is therefore important for any numerical study to examine the sensitivity of each grid resolution on certain flow properties in order to confirm that the final results attained are accurate and reliable.

The CFD community has established that error from the numerical simulation is not only caused by grid convergence error, but also by other factors. However, the total error can be minimized by reducing the error due to grid dependence and this must be done systematically. This leads to the main objective of the study, which is to assess grid independence of flow around a generic train model by using numerical methods, namely an unsteady RANS combined with the SST k-ω turbulence model. Three levels of grid resolutions are used to check the sensitivity of simulation results. In theory, a higher grid resolution increases the total grid cells of the computational domain and reduces simulation time. Consequently, the spatial discretization errors will asymptotically approach zero except for the computer round-off error. The level of grid independence is then systematically evaluated using Richardson extrapolation and the Grid Convergence Index (GCI). Additionally, by optimizing simulation time through the study of grid convergence, the impact on computational costs can be reduced.

In this study, version 2.3.x of the OpenFOAM CFD software package is used to numerically analyze the fluid flow characteristics surrounding a generic train model. OpenFOAM is a free, open source software package that is capable of simulating a wide variety of fluid processes. With an extensive range of features that are contributed voluntarily by the CFD community around the world, OpenFOAM has the capabilities to simulate a wide range of flow-related problems. Based on Robertson *et al.* (2015), there are over 170 utilities available for various purposes such as mesh generation, pre-processing and post-processing. OpenFOAM is an alternative to other commercial

CFD packages and it is increasingly well known to academic researchers and industrial practitioners. In the past few years, there are several notable studies that have been published by OpenFOAM users worldwide in the fields of computational fluid dynamics (CFD), computational heat transfer, fluid structure interaction and multiphase flow.

This article is organized as follows: The descriptions of the train is presented in Section 2. The numerical wind tunnel is explained in Section 3 and mesh description is included in Section 4. In Section 5, the numerical setting is explained. Results and discussion, both of which are divided into the grid convergence study, as well as comparison with previous studies are presented in Section 6. The computing machine for the simulations is then reported in Section 7 to evaluate the computational cost required to simulate all cases. Finally, conclusion is given in Section 8.

2. Model description

The model used in this study is a generic train model which replicates a similar model investigated in the experiment by Sakuma *et al.* (2009) and simulation by Osth *et al.* (2012) as shown in Figs. 1 and 2. Geometric configurations of the train model are listed below:

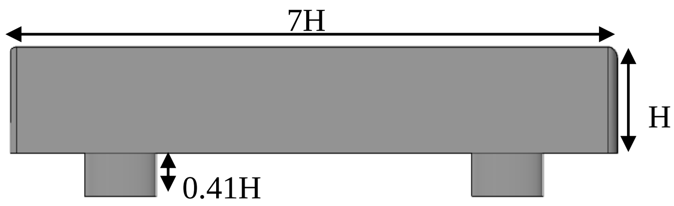

Fig. 1 Side view of the train model

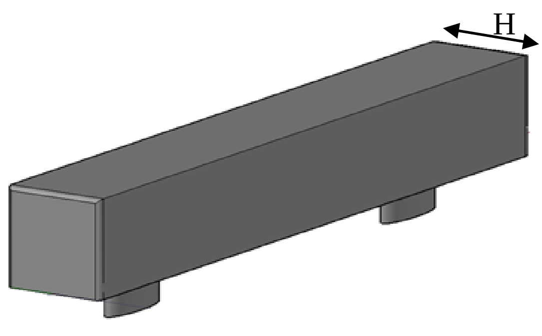

Fig. 2 Isometric view of the train model

Fig. 3 Rounded corners of the train model (a) front corner elliptical rounding and (b) rear corner circular rounding

a. Leading top and side edges on the front are rounded following an elliptical profile as shown in Fig. 3(a). The lengths of the major and minor axes are 0.07H and 0.04H, respectively.
b. The top and side edges on the rear end of the bluff body are rounded with a circular radius of 0.107H as shown in Fig. 3(b).
c. Both front and rear bottom edges are not rounded (sharp edges).
d. The model is placed on two egg-shaped supports and is lifted 0.41H above the ground in order to replicate the same condition as in the wind tunnel study of Sakuma *et al.* (2009).

The length of the train is 7H while the width (w) is equal to the height (h) of the train i.e., 0.56 m.

3. Numerical wind tunnel description

The dimension of the numerical wind tunnel is 36H × 21H × 11.41H ($l \times w \times h$). The distance from the inlet to the bluff body is 8H and the distance from the bluff body to the outlet is 21H. These lengths were found to be sufficient in previous simulations of flows around a simplified train models by Hemida *et al.* (2005), Krajnovic and Davidson (2004), Hemida and Krajnovic (2010).

Boundary conditions of the numerical wind tunnel were selected based on simulation works done by Osth *et al.* (2012). This is to form the turbulent flow and to put the train model within the layer of logarithmic law that represents the completely developed flow. Uniform velocity, which represents the free stream velocity (U_∞) in the *x*-direction, is fixed at the inlet condition to drive wind flow through the internal domain. The slip condition is imposed on the ground plane in order to prevent the development of a boundary layer and to replicate the relative movement between the train and the ground. The homogenous Neumann boundary condition is applied at the outlet. Lastly, the slip condition is also applied on the lateral sides and roof of the train model. Details of the domain and its boundary conditions are illustrated in Figs. 4 and 5.

The Reynolds number (Re) used in this paper is 3.7×10^5 $(Re = U_\infty H/\upsilon)$, based on train height H, kinematic viscosity υ, and free stream velocity U_∞. This particular Reynolds number is selected in order to validate the simulation done in a previous work by Osth *et al.* (2012).

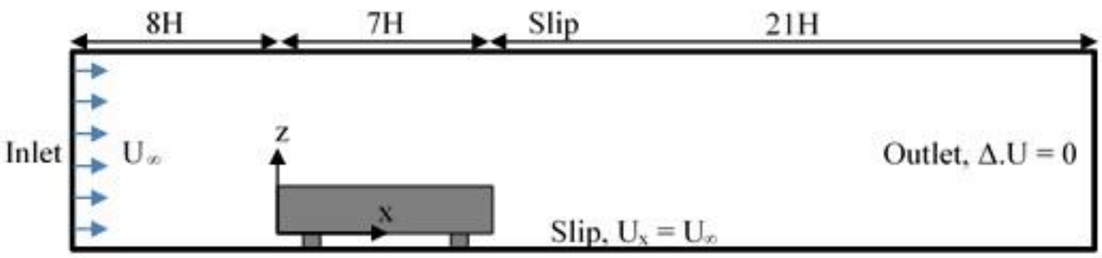

Fig. 4 Computational domain used in the numerical investigation: Side View

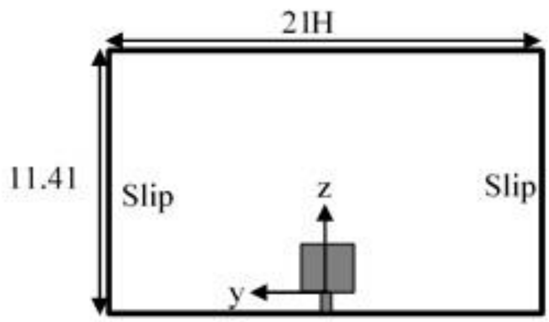

Fig. 5 Computational domain used in the numerical investigation: Front View

4. Mesh description

The cells in the numerical wind tunnel were constructed using a structured non-uniform Cartesian mesh by using *blockMesh*, which is a primary meshing tool in the OpenFOAM software. Additional mesh refinement was applied near the train surface and its surrounding areas using the mesh generation utility of the *SnappyHexMesh* tool, which was also supplied with the OpenFOAM. Three types of grid resolutions i.e., fine, medium and coarse grids were used in this study. These different grid resolutions were selected based on the grid refinement ratio (r). According to Celik *et al.* (2008), a desirable value of r is greater than 1.3 in order to optimize the accuracy of turbulent flow prediction. Since the meshes are not uniform, the grid refinement ratio was calculated based on average grid size(h_{ave}). Details of the meshes can be seen in Table 1.

Referring to Celik *et al.* (2008), the grid refinement ratio (r) and the average cell size (h_{ave}) can be calculated as follows

$$r_{21} = \frac{h_2}{h_1} \tag{1}$$

$$r_{32} = \frac{h_3}{h_2} \tag{2}$$

$$h_{ave} = \left[\frac{1}{N}\sum_{i=1}^{N}(\Delta V_i)\right]^{\frac{1}{3}} \tag{3}$$

where ΔV_i is the volume of the i^{th} cell, and N is the total number of cells.

Wall function is used in all cases to reduce computational cost by properly treating the cell size near the surface. This will minimize the overall number of grids, especially at near-wall regions while maintaining the accuracy of the computational result. The distance of the first cell layer to the model surface should be located within the requirements of y^+ ($30 < y^+ < 300$). Fig. 6 shows a cross section of mesh generation for Case A. Fig. 7 shows y^+ value along the surface centerline of the train, from which Case A (Fine) demonstrates a much lower y^+distribution compared to other coarser grids

Table 1 Grid parameters for cases A, B and C where the subscripts 1, 2 and 3 represent case A, B and C respectively

CASE	A (Fine)	B (Medium)	C (Coarse)
Total No. of Cells, N	2,114,715	951,838	359,838
Average cell size, h_{ave}(m)	0.0895	0.1168	0.1615
Average y^+	81.76	83.28	113.59
Refinement ratio, r	$r_{21} = 1.31$		$r_{32} = 1.38$

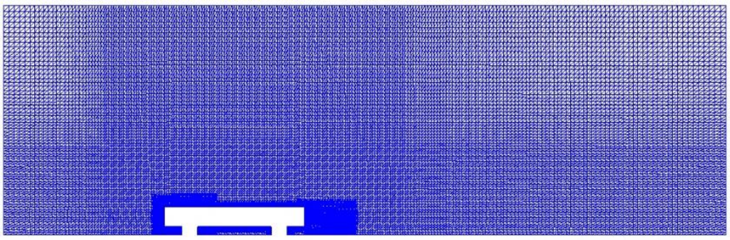

(a)

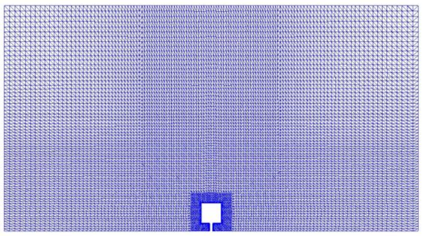

(b)

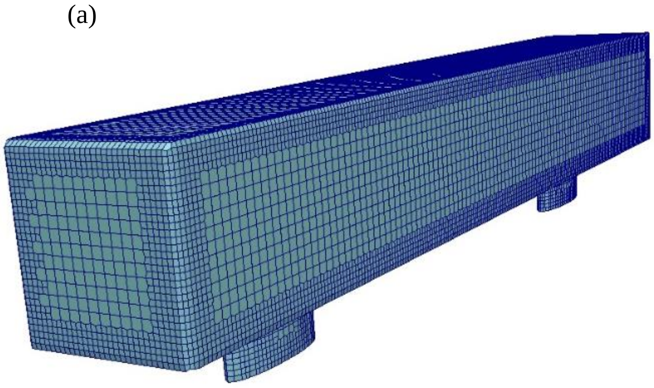

(c)

Fig. 6 Detail of mesh for Case A. (a) at middle plane cross-section, (b) at 1H from front nose cross-section and (c) on the train model

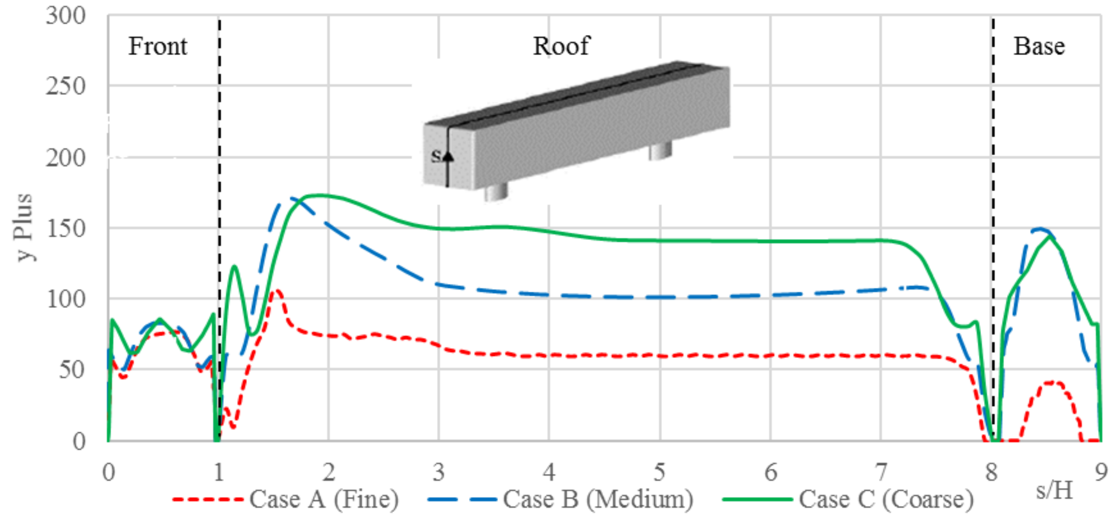

Fig. 7 Distribution of y^+ along the surface centreline of the train

Table 2 Numerical methods used in OpenFOAM

Discretization		Scheme	Description
Time		Backward difference	2^{nd} order implicit
Spatial	Gradient	Central differencing	2^{nd} order central differencing
	Divergence	QUICKV	3^{rd} order
	Laplacian	Gauss linear differencing scheme	2^{nd} order unbounded
Pressure-velocity coupling		PISO	Used as transient algorithm
Turbulence models	URANS	$k-\omega$	Shear-Stress-Transport (SST)
Wall functions	k	*kqRWallFunction*	Act as a zero-gradient condition for modelled k
	ω	*omegaWallFunction*	Automatic wall functions condition for ω
	ν_t	*nutkWallFunction*	Generates near-wall profile for ν_t based on modelled k

5. Numerical setting

The primitive variables were calculated numerically based on three dimensional unsteady incompressible Navier-Stokes and continuity equations. The flow around the train as considered incompressible and obtained by solving the incompressible form of the URANS equation combined with the help of turbulent model. The pressure implicit split operator (PISO) solution algorithm based on Barton (1998) with one predictor step and two corrector steps for pressure-velocity coupling was used to solve the transient problems in this study. The discretization schemes used were at least in the second-order accuracy and this was applied to all equations. Table 2 summarizes the details of the numerical methods used.

Three different time steps were used, corresponding to the three different grid cases, so that the Courant-Fredichs-Lewy (CFL) number always remained below unity. Table 3 shows the time step for pressure, convection and diffusion terms, Δt for each case.

5.1 Governing equations

The URANS equations were principally obtained from the RANS equation, but the unsteady term was maintained. The governing equations, namely the continuity and Navier-Stokes equations for the incompressible flows, are

$$\frac{\partial u_i}{\partial x_i} = 0 \tag{4}$$

$$\rho \frac{\partial u_i}{\partial t} + \rho U_j \frac{\partial u_i}{\partial x_j} = -\frac{\partial p_i}{\partial x_j} + \frac{\partial}{\partial x_j}\left[\mu\left(\frac{\partial u_j}{\partial x_j} + \frac{\partial u_i}{\partial x_j}\right)\right] \tag{5}$$

The velocity components, u_i and the pressure, p_i are both nonlinear partial differential equations. This means that there is no analytical solution for the problem with arbitrary boundary conditions. The unsteadiness of the flow variables (i.e., velocity and pressure) were decomposed into mean value and fluctuation terms as follows

$$u_i = U_i + u_i' \tag{6}$$

$$p_i = P_i + p'_i \tag{7}$$

where U_i and P_i are the time-averaged terms, while u_i' is the fluctuation term for velocity and p_i' is the fluctuation term for pressure.

Substituting these Reynolds decomposed velocities and pressures into the continuity and Navier-Stokes equations yields the Reynolds Averaged Navier-Stokes equation of motions as shown below

$$\frac{\partial U_i}{\partial x_i} = 0 \tag{8}$$

$$\frac{\partial U_i}{\partial t} + U_j \frac{\partial U_i}{\partial x_j} = -\frac{1}{\rho}\frac{\partial P_i}{\partial x_i} + \frac{\partial}{\partial x_j}\left(\mu \frac{\partial U_i}{\partial x_j} - \rho\overline{u_i' u_j'}\right) \tag{9}$$

Table 3 Time step for case A, B and C

CASE	A(Fine)	B(Medium)	C(Coarse)
Δt	0.002	0.003	0.005

5.2 Turbulence model

For a URANS simulation, in order to solve the governing equations, the Reynolds stress tensor $-\rho\overline{u_i'u_j'}$ must first be determined. The Reynolds stress can be modelled by additional equations or from the known quantities in order to achieve "closure" for the governing equations. Closure denotes that there is a sufficient number of equations for all the unknowns, including the Reynolds stress tensor that resulted from the averaging procedure. The equation is used to close the system, depending on the turbulence model.

A turbulence model is a computational procedure to close the system of flow equations as derived earlier. Most of them are based on the Boussinesq hypothesis which links the Reynolds stress tensor to the mean rate of deformation. The most widely used concept is

$$-\rho\overline{u_i'u_j'} = \mu_t\left(\frac{\partial U_i}{\partial x_j} + \frac{\partial U_j}{\partial x_i} - \frac{2}{3}\frac{\partial U_k}{\partial x_k}\delta_{ij}\right) - \frac{2}{3}\rho k\delta_{ij} \tag{10}$$

where the turbulent kinetic energy (k) and the specific dissipation rate (ω) are solved using the following equations

Turbulence Kinetic Energy, k

$$\frac{\partial k}{\partial t} + U_j\frac{\partial k}{\partial x_j} = P_k - \beta^* k\omega + \frac{\partial}{\partial x_j}\left[(\nu + \sigma_k\nu_T)\frac{\partial k}{\partial x_j}\right] \tag{11}$$

Specific Dissipation Rate, ω

$$\frac{\partial \omega}{\partial t} + U_j\frac{\partial \omega}{\partial x_j} = \alpha S^2 - \beta\omega^2 + \frac{\partial}{\partial x_j}\left[(\nu + \sigma_\omega\nu_T)\frac{\partial \omega}{\partial x_j}\right] + 2(1 - F_1)\sigma_{\omega 2}\frac{1}{\omega}\frac{\partial k}{\partial x_i}\frac{\partial \omega}{\partial x_i} \tag{12}$$

where ν_T is the kinematic eddy viscosity which is defined as follows

$$\nu_T = \frac{a_1 k}{\max(a_1\omega, SF_2)} \tag{13}$$

The following closure coefficient used in this study is

$$F_2 = \tanh\left[\left[\max\left(\frac{2\sqrt{k}}{\beta^*\omega y}, \frac{500\nu}{y^2\omega}\right)\right]^2\right] \tag{14}$$

where *y* is the distance to the next surface

$$P_k = \min\left(\tau_{ij}\frac{\partial U_i}{\partial x_j}, 10\beta^* k\omega\right) \tag{15}$$

$$F_1 = \tanh\left\{\left\{\min\left[\max\left(\frac{\sqrt{k}}{\beta^*\omega y}, \frac{500v}{y^2\omega}\right), \frac{4\sigma_{\omega 2}k}{CD_{k\omega}y^2}\right]\right\}^4\right\} \tag{16}$$

$$CD_{k\omega} = \max\left(2\rho\sigma_{\omega 2}\frac{1}{\omega}\frac{\partial k}{\partial x_i}\frac{\partial \omega}{\partial x_i}, 10^{-10}\right) \tag{17}$$

$$\phi = \phi_1 F_1 + \phi_2(1 - F_1) \tag{18}$$

$$\alpha_1 = \frac{5}{9}, \alpha_2 = 0.44 \tag{19}$$

$$\beta_1 = 0.075, \beta_2 = 0.0828, \beta^* = 0.09 \tag{20}$$

$$\sigma_{k1} = 0.85, \sigma_{k2} = 1, \sigma_{\omega 1} = 0.5, \sigma_{\omega 2} = 0.856 \tag{21}$$

6. Results and discussions

6.1 Grid convergence study

6.1.1 Richardson extrapolation

Richardson extrapolation by Richardson *et al.* (1924) is a method of obtaining a higher-order estimate of the continuum value (value at zero grid spacing) from a series of lower-order discrete values. In grid refinement studies, the estimated value is obtained if the cell grid size tends to zero $(h \rightarrow 0)$. Extrapolation is made from the results of at least two different grid solutions. However, for a convergence study, Stern *et al.* (2001) proposed a minimum of three grid solutions. Roache (1994) generalized the Richardson extrapolation by introducing the p^{th}-order methods

$$f_{RE} \approx f_1 + [(f_1 - f_2)/(r^p - 1)] \tag{22}$$

where r is the refinement ratio as shown in Eqs. (1) and (2).

From Table 1, the refinement ratio between successive grid resolutions were not constant $(r_{21} \neq r_{32})$. Thus, the extrapolated value differs by changing the order of accuracy (p) and this can be estimated by using the equation below

$$p = \frac{1}{\ln(r_{21})}\left|ln\left|{}^{\varepsilon_{32}}/_{\varepsilon_{21}}\right| + q(p)\right| \tag{23}$$

$$\varepsilon_{32} = f_3 - f_2 \tag{24}$$

$$\varepsilon_{21} = f_2 - f_1 \tag{25}$$

$$q(p) = ln\left(\frac{r_{21}^{p} - s}{r_{32}^{p} - s}\right) \tag{26}$$

$$s = 1.\, sign\left({}^{\varepsilon_{32}}/_{\varepsilon_{21}}\right) \tag{27}$$

Note that $q(p) = 0$ for the constant value of r (i.e., $r_{21} = r_{32}$). However, convergence conditions must be first determined in order to evaluate the extrapolated value of these solutions. In total, there are basically three possible convergence conditions

a. $(0 < R < 1)$ for monotonic convergence

b. $(R < 0)$ for oscillatory convergence

c. $(R > 1)$ for divergence

where the convergence ratio (R) is defined as follows

$$R = \frac{\varepsilon_{21}}{\varepsilon_{32}} \tag{28}$$

6.1.2 Grid Convergence Index (GCI)

According to Roache (1994), GCI delivers a consistent manner in reporting the results of convergence solutions for grid refinement studies. The method is based upon a grid refinement error estimator derived from the theory of generalized Richardson extrapolation. The GCI value indicates the percentage in which the computed value is away from the value of the asymptotic numerical value. It shows an error band showing the deviation of the solution from the asymptotic value and changes of the solution with a further refinement of the grid. A small value of GCI indicates that the computation is in the asymptotic range. Similar to the Richardson extrapolation, a minimum of two levels of grid required for the GCI computation. However, three levels are suggested in order to precisely calculate the order of convergence and to check that the solutions are within the asymptotic range of convergence. The GCI for the fine grid solution is defined as

$$GCI_{i+1,i} = F_s \frac{\left|\varepsilon_{i+1,i}\right|}{f_i(r^p - 1)} \times 100\% \tag{29}$$

where the safety factor (F_s) for the three grids is 1.25 following Wilcox (2006). The discrepancy between the simulation value and the extrapolated value based on Richardson extrapolation can be used to define the percentage error

$$E_i = \left|\frac{f_i - f_{RE}}{f_{RE}}\right| \times 100\% \tag{30}$$

Table 4 shows the result of different parameters obtained from the simulation of different mesh resolutions and corresponding extrapolated values based on Richardson extrapolation. Table 5 summarizes the GCI analysis of these results. Based on the outcome, the convergence criteria are monotonic since $0 < R < 1$ for all cases.

For each parameter, the result of the grid convergence study is presented in two types of graphs. The first graph (Figs. 8, 11, 13 and 15) visualize the changes of each parameter from different grid resolutions with the extrapolated value based on Richardson extrapolation. In contrast, the second graph (Figs. 9, 12, 14 and 16) shows the percentage error for each parameter based on Eq. (30).

a)Mean drag coefficient (C_D)

The global parameter of mean C_D can be seen in Figs. 8 and 9, compared to the extrapolated value derived in f_1/f_{RE}= 0.9992. This corresponds to the minimum error of E_1 = 0.089% for the fine grid mesh as compared to the extrapolated value. The percentage of error improves by a maximum of 3% ($E_3 - E_1$). In addition, the GCI for the fine grid resolution, namely GCI_{21} is 0.1122%, is rather low, such that further refinement of this fine grid resolution will not impact the final value of mean C_D.

Table 4 Comparison of different parameter results between different mesh resolutions and the extrapolated value calculated using Richardson extrapolation

CASE	A(f_1)	B(f_2)	C(f_3)	f_{RE}
C_D mean	0.7248	0.7222	0.7031	0.7254
Stagnation Pressure (Nm)	0.4918	0.4910	0.4884	0.4923
Base Pressure (10^{-3}) (Nm)	-4.0654	-4.1272	-4.3692	-4.0308
Wake Length (m)	0.5764	0.5723	0.5482	0.5778

Table 5 Grid Convergence Index (GCI) for different parameters

CASE	$\lvert\varepsilon_{32}\rvert$ (10^{-2})	$\lvert\varepsilon_{21}\rvert$ (10^{-2})	R	GCI_{32} (%)	GCI_{21} (%)
C_D mean	1.91	0.26	0.133	0.5542	0.1122
Stagnation Pressure	0.26	0.08	0.2932	0.3262	0.1307
Base Pressure	0.0242	0.0062	0.255	2.9056	1.0496
Wake Length	2.4068	0.4101	0.170	1.1946	0.2969

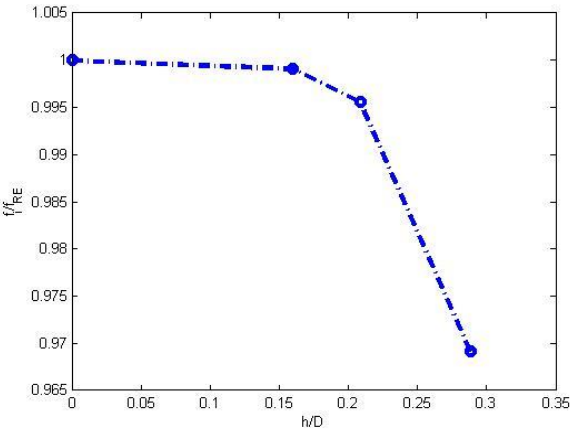

Fig. 8 Comparison of mean C_D normalized by the extrapolated, between three grid solutions and Richardson extrapolation estimation. f_1/f_{RE}= 0.9992, f_2/f_{RE}= 0.9956 and f_3/f_{RE}= 0.9693

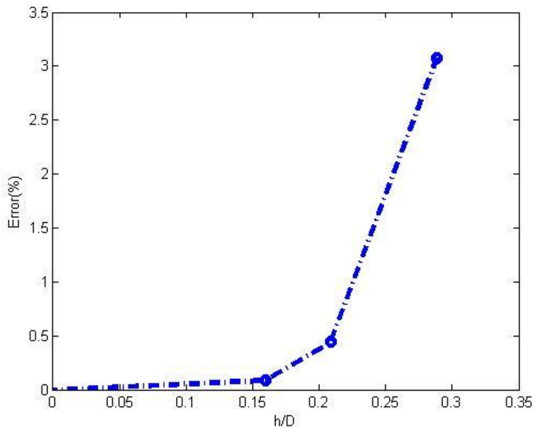

Fig. 9 Percent of error for mean C_D for three grid resolutions. E_1 = 0.089%, E_2 = 0.441% and E_3 = 3.079%

b)Stagnation pressure

Secondly, a comparison for the local parameter of stagnation pressure is shown in Figs. 11-12. By definition, a stagnation pressure is the static pressure at a stagnation point in a fluid flow. Stagnation pressure is equal to the sum of the free-stream dynamic pressure and free-stream static pressure. In this case, the stagnation pressure is obtained at the point located at the center on the front of the train model (Fig. 10). The result shows that as the grid is refined, the discrepancy between the solution and the extrapolated value decreases. Hence, the ratio between finer mesh data with the extrapolated value is almost at unity, f_1/f_{RE}= 0.9989. This results in a small error of E_1 = 0.105% and a corresponding GCI for the fine grid resolution of GCI_{21} = 0.1307%.

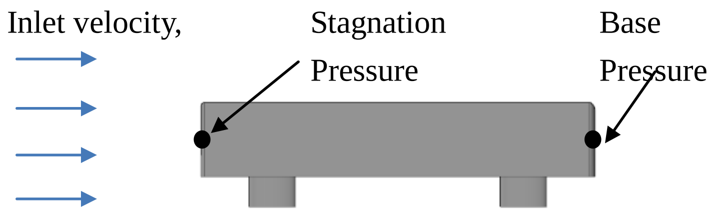

Fig. 10 Location of data acquired for stagnation pressure and base pressure

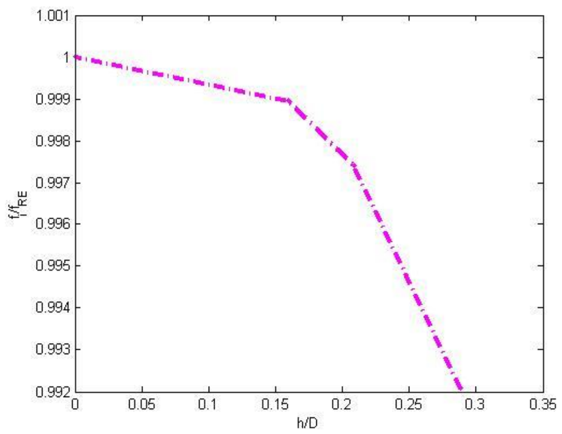

Fig. 11 Comparison of stagnation pressure normalized by the extrapolated, between three grid solutions and Richardson extrapolation estimation. f_1/f_{RE} = 0.9989, f_2/f_{RE} = 0.9974 and f_3/f_{RE} = 0.9921

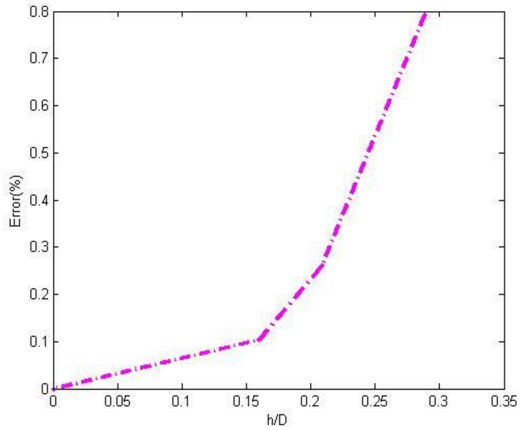

Fig. 12 Percent of error for stagnation pressure for three grid resolutions. E_1 = 0.105%, E_2 = 0.260% and E_3 = 0.792%

c) Base pressure

A similar behavior is observed in the point parameter of base pressure (Figs. 13 and 14) which is attained at the center of the train model's rear end (Fig. 10). From the result, from coarser to finer grid resolution, a converging data pattern towards the extrapolated value was achieved with the finest grid mesh resulting in f_1/f_{RE}= 1.0164, E_1 = 0.848% and GCI_{21}= 1.0496%.

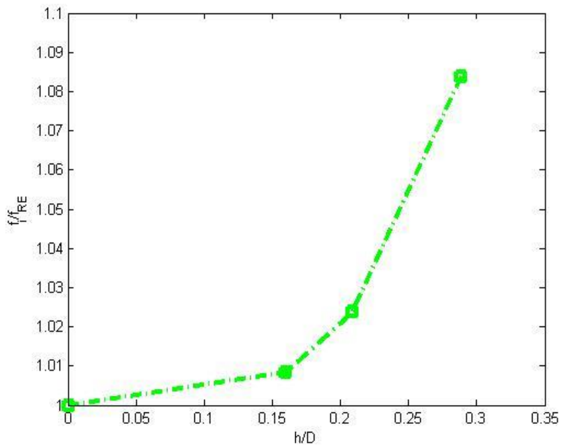

Fig. 13 Comparison of base pressure normalized by the extrapolated, between three grid solutions and Richardson extrapolation estimation. f_1/f_{RE}= 1.0164, f_2/f_{RE}= 1.0318 and f_3/f_{RE}= 1.0923

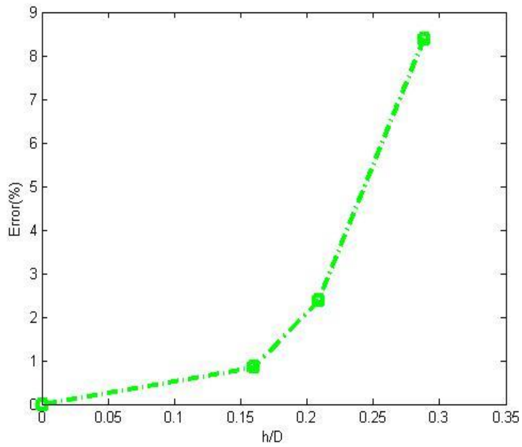

Fig. 14 Percent of error for base pressure for three grid resolutions. E_1 = 0.848%, E_2 = 2.381% and E_3 = 8.384%

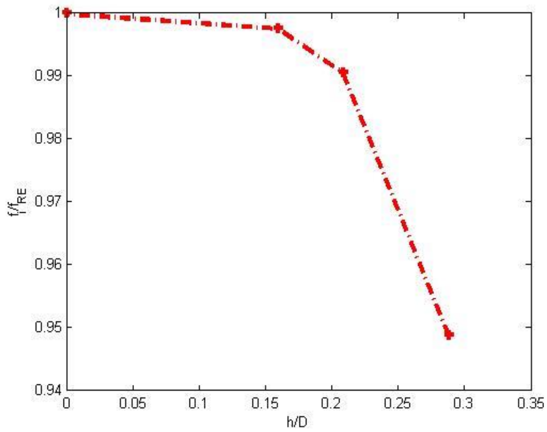

Fig. 15 Comparison of wake length normalized by the extrapolated, between three grid solutions and Richardson extrapolation estimation. f_1/f_{RE}= 0.9976, f_2/f_{RE}= 0.9905 and f_3/f_{RE}= 0.9488

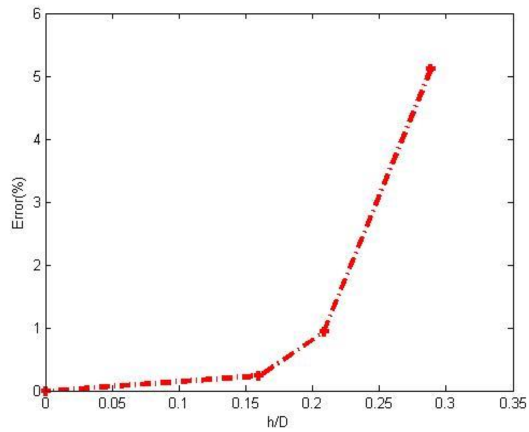

Fig. 16 Percent of error for wake length for three grid resolutions. E_1 = 0.238%, E_2 = 0.947% and E_3 = 5.113%

d) Wake length

Lastly, a comparison was also made for the wake length (Figs. 15 and 16) which is defined as the region of flow recirculation immediately behind a moving or stationary blunt body caused by viscosity (refer Figs. 20 and 22 for details of the wake flow structures). Since it is already mentioned earlier that monotonic convergence criteria was achieved in this case, the successive grid refinements nearly achieved the asymptotic value at the finest grid resolution, where $E_{1,}$ was only 0.238% with f_1/f_{RE}= 0.9976. The corresponding GCI value for the fine grid resolution, GCI_{21} was 0.2969%.

In general, very low values of percentage error (E_i) were attained for the finer grid resolution (case A). For the GCI analysis, there was a reduction in the GCI values for the successive grid refinements ($GCI_{21} < GCI_{32}$). Based on Ali *et al.* (2009), when the GCI for finer grid (GCI_{21}) was comparatively low as compared to the coarser grid (GCI_{32}), it indicated that the dependency of the numerical simulation on cell size was reduced. Most of the parameters produced a GCI_{21} of less than 1%, except for the base pressure point parameter. This suggests that the finer grid approached an asymptotic value, where the error due to the spatial discretization was reduced significantly. Furthermore, since the GCI reduction from the coarser grid to the finer grid is relatively significant, the grid independence solution can be deduced to have been nearly achieved. Therefore, any further refinement of the grid would not have much impact on the flow simulation results.

6.2 Comparison of numerical data from case A with previous studies

Changes in pressure and velocity fields occur in the external flow of fluids around bodies. It is of great importance to consider the characteristics of the flow when designing and constructing bodies exposed to external flows. This section presents details of pressure distribution, streamlines and global parameter (i.e., mean drag force coefficient) when the flow passes a bluff body which in this case is a generic train model.

6.2.1 Pressure coefficients

For comparison purposes, the results obtained from Case A (fine mesh) were compared with the previous experimental data by Sakuma *et al.* (2009) and numerical data by Osth *et al.* (2012). Firstly, pressure coefficient was selected and defined as

$$C_p = (p - p_\infty / 0.5\rho U_\infty^2) \tag{31}$$

where p is the local static pressure and p_∞ is the free stream static pressure.

The pressure coefficient along the centerline of the train model for the case study using the SST $k-\omega$ turbulence model is shown in Fig. 17. In general, the pressure follows the same pattern as the results of Sakuma *et al.* (2009) and Osth *et al.* (2012). However, discrepancies occurred at the separated flow region (s/H = 1) on the front roof of the train. Recent work seems to underestimate the negative pressure at this specific point. From the simulation, the flow reattached further downstream as compared to previous simulation and experimental results. However, a significant similarity was observed in the reattachment region as the flow passed through the roof. In the wake region, a recent simulation slightly underestimated the pressure coefficient value, but it still captured the lowest peak value of pressure coefficient similar to Osth *et al.* (2012).

Furthermore, Fig. 17 also shows the difference in the simulation results for different turbulence models applied. The results of pressure coefficients plotted along the centerline of the train model clearly show better results when using SST $k-\omega$ as compared to other turbulence models. Even though the difference in the values of pressure drop was quite significant at the leading edge, the recovery of pressure towards the rest of the train surface at the top area was more stable and nearer to the one obtained from that of Osth *et al.* (2012). Standard $k-\omega$ clearly underestimated the pressure, especially at the front surface by half of the values recorded using other turbulence models. This conventional $k-\omega$ also underestimated the pressure coefficient at the separation region after the flow passed through the leading edge of the train as well as under the prediction value at Region 3. For the case study with the Realizable $k-\varepsilon$ model, the pressure drop at the leading edge instantly magnified after the flow passed through the leading edge. Additionally, pressure recovery after the sudden drop at the leading edge was also unable to follow as per the validation paper by Osth *et al.* (2012). Lastly, a case study with the one-equation model Spalart Allmaras tended to over-predict most of the pressure coefficient values since it has limitations to accurately compute fields that exhibit shear and separated flows. Based on Ishak *et al.* (2016), a simulation of this type of a turbulence model does not consider the diffusion and convection of turbulent energy and thus, the solution can be achieved more quickly than other types of turbulence models.

Moreover, the similar study of Prime *et al.* (2014) shows good comparison between the results of the SST $k-\omega$ turbulence model and the experiment. In their numerical study on flow modelling of interacting prisms, both the flow velocity and turbulence intensity in various positions in the wake are compared with the experimental data measured using hot-wire and the results show a good agreement for both approaches.

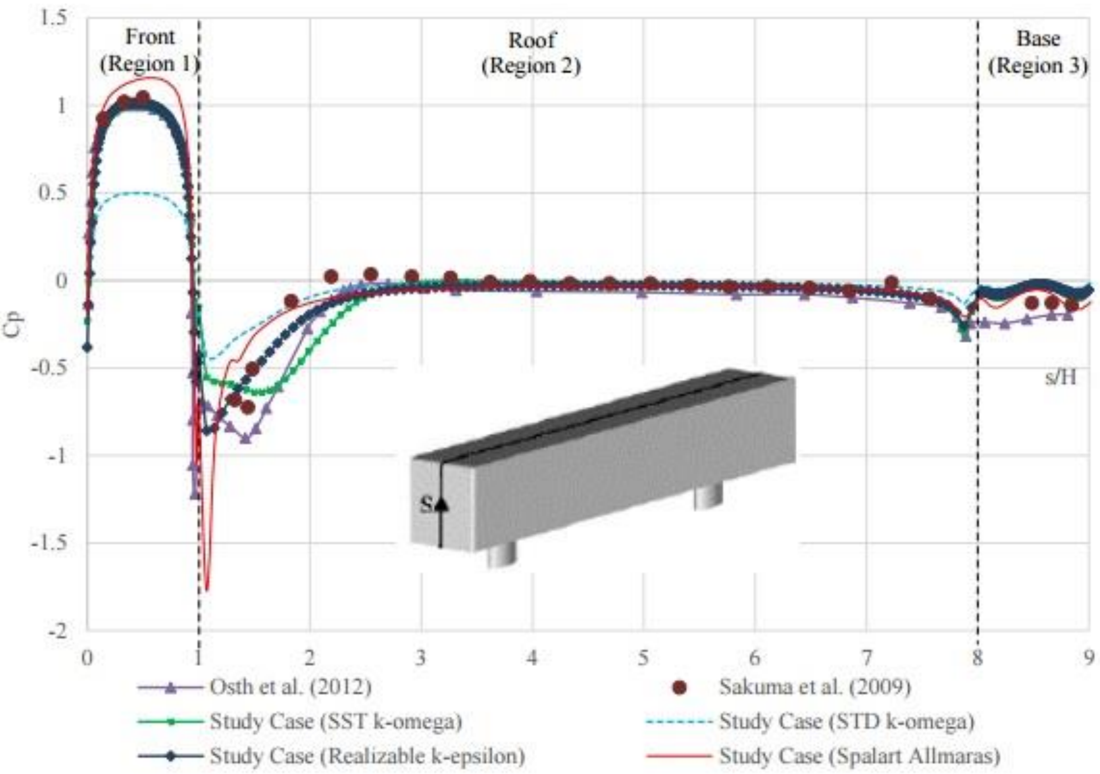

Fig. 17 Pressure coefficient along the centerline of the train model

6.2.2 Global quantity

The time-averaged drag force coefficients from the simulations were compared with those of Osth *et al.* (2012) and Sakuma *et al.* (2009). The results are presented in Table 6. The time-signal of the drag force coefficients for Case A is visualized in Fig. 18. The averaging in simulation was done from 200 time steps after a statically stable condition of up to 1000 time steps was achieved. The drag force coefficient is defined as follows

$$C_D = \frac{2F_D}{\rho U_\infty^2 A_x} \tag{32}$$

where ρ is the density of air at 20℃ and $A_x = H^2$.

Table 6 Simulation settings of the current case studies and the simulation of Osth *et al*. (2012)

CASE	Osth *et al.* (2012)	Study Case
Simulation model	PANS (Partially Averaged Navier Stokes)	URANS (Unsteady Reynolds Averaged Navier Stokes)
No. of extra transport equations	Four model equations $(k - \epsilon - \zeta - f)$[a]	(i) Two model equations • STD $k - \omega$[a] • SST $k - \omega$[a] • Realizable $k - \varepsilon$[a] (ii) One model equation • Spalart Allmaras
Algorithm	SIMPLE (Semi-Implicit Method for Pressure Linked Equations)	(i) SIMPLE (Semi-Implicit Method for Pressure Linked Equations) (ii) PISO (Pressure Implicit with Splitting of Operator)
Time step (physical time)	0.00015	0.002 (CFL < 1)[b]
Time step (convective time unit)	0.00038	0.00051
No. of cells	12 million	2 million

[a] where k is the turbulence kinetic energy, ϵ is the dissipation in the flow, ζ is the scale ratio (e.g., ζ_u is the velocity scale ratio), f is the ratio (e.g., f_ϵ is the ratio of unresolved dissipation to resolve), ω is the specific dissipation rate and ε is the turbulent dissipation.

[b] CFL is the Courant-Fredichs-Lewy condition which must be kept below unity.

Table 7 Drag force coefficient for comparison

Aerodynamic coefficient	Mean C_D
Experiment by Sakuma *et al*. (2009)	0.86
Numerical by Osth *et al*. (2012)	0.78
Study Case (SST *k-ω*)	0.73
Study Case (STD *k-ω*)	0.71
Study Case (Realizable *k-ε*)	0.69
Study Case (Spalart Allmaras)	0.94

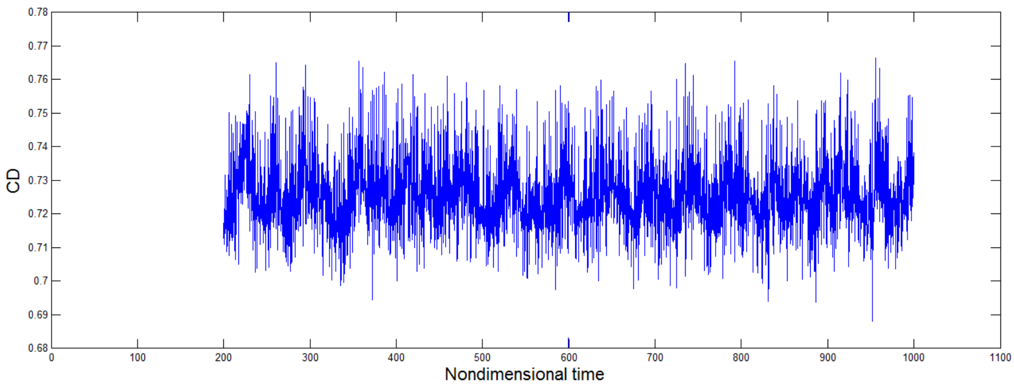

Fig. 18 Time-signal of the drag force coefficients for Case A

Based on Table 7, the mean drag force coefficient (C_D mean) obtained by SST $k-\omega$ was relatively underestimated compared to that of Osth *et al.* (2012) by 6%. The under-prediction of the negative pressure that occurred in the separated region on the roof from Fig. 17 might be one of the reasons that caused discrepancies in the results of mean drag force coefficient with previous works. This is due to the fact that the separation region that starts from the front leading edge actually extends much longer, hence resulting in negative pressure that contributes to a decrease in the total drag coefficient of the train model. Based on Higuchi et al. (2006), and Gurlek et al. (2008), this shear layer reattachment will directly affect the drag on the model.

Table 7 also lists down the detailed differences in the mean drag coefficient (C_D mean) values obtained when different turbulence models are applied in the simulation. From the results, SST $k-\omega$ gives the best result compared to others. Almost all models seem to underestimate mean C_D value when the comparison is made with the numerical result obtained by Osth *et al.* (2012). Finally, the one-equation model Spalart Allmaras shows the farthest value of the mean C_D (overestimate value), which undoubtedly claims that this turbulence model is not suitable for this study.

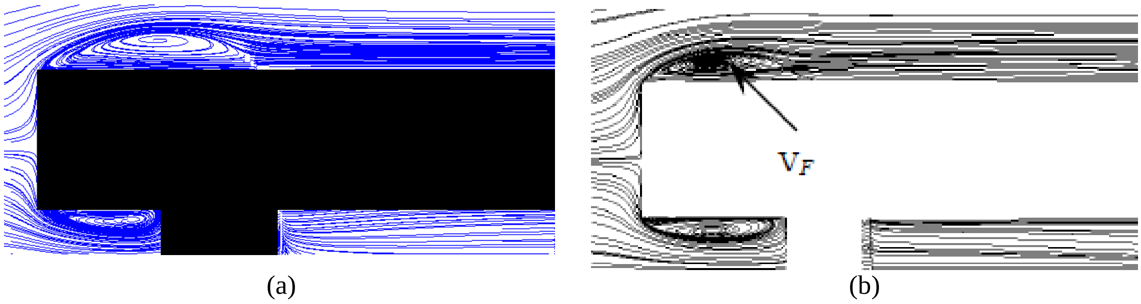

Fig. 19 Side view of streamlines of the time-averaged velocity field around first half of the train where (a) Case A and (b) Osth *et al*. (2012)

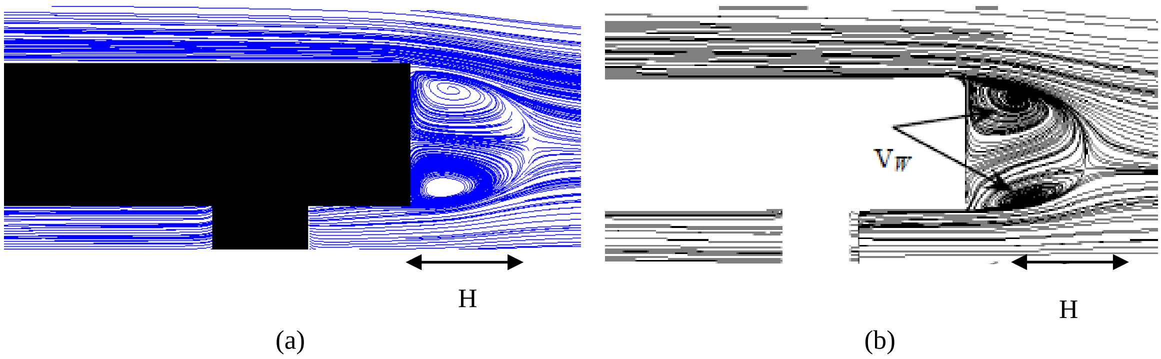

Fig. 20 Side view of streamlines of the time-averaged velocity field around second half of the train where (a) Case A and (b) Osth *et al*. (2012)

6.2.3 Streamlines of the time-averaged flow

Figs. 19 and 20 shows a side view streamlines of the time averaged velocity field in comparison with previous data obtained by Osth *et al*. (2012). As mentioned earlier, only Case A (Fine) is presented here. In general, the current simulation is able to replicate the flow phenomena as obtained by Osth *et al*. (2012).

Fig. 19 shows that flow separation occurred at the front leading edge at the top and bottom sides, and the vortex produced due to this is denoted as V_F. Only a small discrepancy in the size of vortex appeared on the roof of the train model which is a bit larger than that attained by Osth *et al*. (2012). This confirms the earlier argument that the flow reattached further back, resulting in the lower drag force coefficient, C_D than that of Osth *et al*. (2012).

On the other side, a similar flow structure produced at the second half of the train can be seen in Fig. 20. There are two vortices at the upper and bottom sides forming in the wake and denoted as V_w. The result of Case A agrees well with previous simulation data, with vortex V_w extending about a distance H in the streamwise direction from the base. Accurately, this wake length for Case A is equal to 0.5764 m which extends about 1.03H from the rear end surface of the train model (refer Table 4).

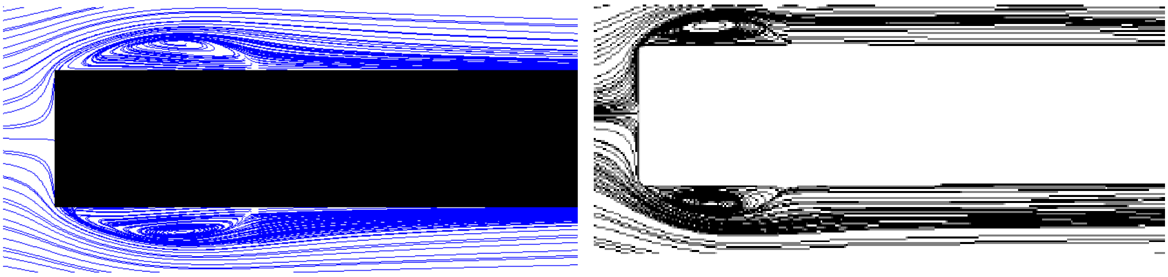

(a) (b)

Fig. 21 Top view of streamlines of the time-averaged velocity field around first half of the train (a) Case A and (b) Osth *et al*. (2012)

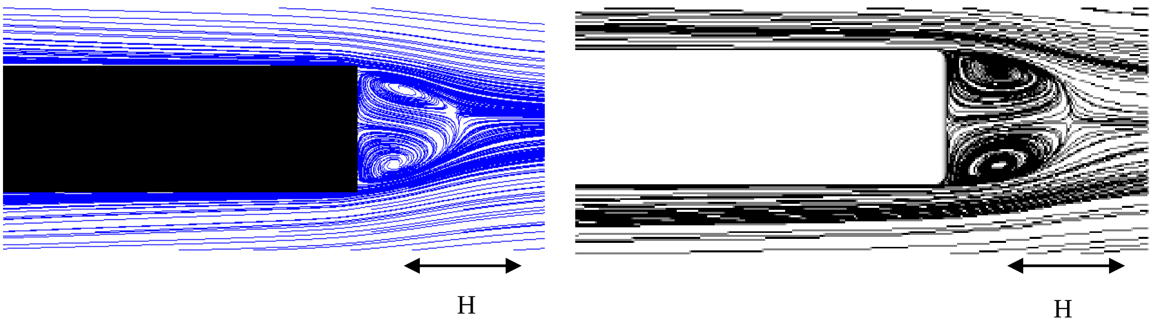

(a) (b)

Fig22 Top view of streamlines of the time-averaged velocity field around second half of the train (a) Case A and (b) Osth *et al*. (2012)

Figs. 21 and 22 in contrast illustrate the streamlines of the time averaged velocity field comparison from the top view. In Fig. 21, flow separation occurs at both sides of the leading edges and produces vortices which are similar in size. As previously stated, the vortices appear to be slightly extended in the streamwise direction replicating the vortex formation on the top leading edge of the train model.

The flow structure formed at the second half of the train resembles the same shape obtained by Osth *et al*. (2012). There are two vortices forming sideways in the wake. The vortex extends for about a distance H in the streamwise direction from the base of the train.

7. The computing machine

The simulations that were performed used OpenFOAM, exercising the message passing interface (MPI) method by utilizing parallel processors. To run the simulation job in parallel, the computational domain needed to be decomposed into several smaller domains. This was set by using the *decomposePar* utility where the total number of processors to run a particular job was selected. By utilizing parallel processors, running any OpenFOAM job could be made faster. Table 8 shows the performance of the computer in simulating three different grid resolutions, cases A, B and C.

Table 8 Computer performance for different number of processors used in the simulation

CASE	A(Fine)	B(Medium)	C(Coarse)
No. of processors	32	16	8
Clock time (hour)	325	162	78
Simulation time $\left(U_\infty/_H\right)$	1000	1000	1000
Time step (physical time) (Δt)(s)	0.002	0.003	0.005
Time step (convective time units) $\left(\Delta t U_\infty/_H\right)$	0.00051	0.00077	0.00128

8. Conclusions

The flow around a generic train model was simulated numerically using OpenFOAM framework by utilizing Unsteady Reynolds Navier-Stokes (URANS) equation combined with SST $k-\omega$ turbulence model for three different mesh resolutions. The grid independence study based on a systematic assessment of computational grid refinement through the Grid Convergence Index (GCI) and Richardson extrapolation shows a convincing result for finding an optimal grid resolution. Inspection of GCI analysis of the different parameters shows a gradual reduction in values when the grid system is refined. From Richardson extrapolation, the extrapolated value calculated shows that the finer grid (Case A) is appropriate to be used for further analysis as the finest GCI's for most of the parameters being investigated are below 1%.

This article shows that flow structure and flow properties can be captured appropriately with the use of OpenFOAM. Compared to a previous paper, the values of both pressure coefficient and mean drag coefficient were reasonable due to the fact that the amount of grid difference was quite large (~10 million). It is also fair to point out the limitation in URANS' capability of simulating transient flow problems as in this case study. However, with the systematic method in mesh size refining proposed in this study, simulations on any types of fluid flow problems can be conducted properly by implementing the Grid Convergence Index (GCI) and Richardson extrapolation analysis. Provided that the result is comparable, with the mesh resolution used in the current work is much lower than in the previous work, more reasonable simulation time can be achieved. This consequently reduces the computational cost with a justified explanation on the final outcome.

Acknowledgements

This research was financially supported by the Ministry of Higher Education (MOHE) Malaysia under the Research University Grant (RUG) project of Universiti Teknologi Malaysia (FRGS PY/2015/05383 and TWAS 13-272). High Performance Computer (HPC) Universiti Teknologi Malaysia also provided access to their supercomputer facilities.

References

Alam, F. and Watkins, S. (2006), "Crosswind effects on high cube freight trains", *Proceedings of the 3rd BSME-ASME International Conference on Thermal Engineering*, Dhaka, Bangladesh.

Ali, M S.M., Doolan, C.J. and Wheatley, V. (2009), "Grid convergence study for a two-dimensional simulation of flow around a square cylinder at low Reynolds number", *Proceedings of the 7th International Conference on CFD in the Minerals and Process Industries CSIRO*, Melbourne, Australia.

Barton, I.E. (1998), "Comparison of SIMPLE- and PISO-type algorithms for transient flows", *Int. J. Numer. Meth. Fl.*, **26**(4), 459-483.

Biadgo, A.M., Simonovic, A., Scorvan, J. and Stupar, S. (2014), "Aerodynamic characteristics of high speed train under turbulent crosswinds", *J. Modern Transportation*, **22**, 225-234.

Celik, I., Ghia, U., Roache, P.J. and Freitas, C. (2008), "Procedure for estimation and reporting of uncertainty due to discretization in CFD applications", *J. Fluid. Eng. -T ASME*, **130**(7), doi:10.1115/1.2960953.

Chiu, T. (1995), "Prediction of the aerodynamic loads on a railway train in a cross-wind at large yaw angles using an integrated two- and three-dimensional source/vortex panel method", *J. Wind Eng. Ind. Aerod.*, **57**(1), 19-39.

Chiu, T. and Squire, L. (1992), "An experimental study of the flow over a train in a crosswind at large yaw angle up to 90º", *J. Wind Eng. Ind. Aerod.*, **45**(1), 47-74.

Gurlek, C., Sahin, B., Ozalp, C. and Akilli, H. (2008), "Flow structures around a three-dimensional rectangular body with ground effect", *Wind Struct.*, **11**(5), 345-359.

Hemida, H. and Baker, C. (2010), "Large-eddy simulation of the flow around a freight wagon subjected to a crosswind", *Comput. Fluids*, **39**(10), 1944-1956.

Hemida, H. and Krajnovic, S. (2009), "Exploring flow structures around a simplified 30° side wind using LES", *Eng. Appl. Comput. Fluid Mech.*, **3**(1), 28-41.

Hemida, H. and Krajnovic, S. (2010), "LES study of the influence of the nose shape and yaw angles on flow structures around trains", *J. Wind Eng. Ind. Aerod.*, **98**(1), 34-46.

Hemida, H., Krajnovic, S. and Davidson, L. (2005), "Large-eddy simulations of the flow around a simplified high speed train under the influence of cross-wind", *Proceedings of the 17th AIAA Computational Fluid Dynamics Conference*, Toronto, Ontario Canada.

Higuchi, H., Van Langen, P., Sawada, H. and Tinney, C.E. (2006), "Axial flow over a blunt circular cylinder with and without shear layer reattachment", *J. Fluids Struct.*, **22**(6-7), 949-959.

Ishak, I.A., Ali, M.S.M. and Shaikh Salim, S.A.Z. (2016), "Numerical simulation of flow around a simplified high-speed train model using OpenFOAM", *Proceedings of the Aerotech VI Conference: Innovation in Aerospace Engineering and Technology*, Kuala Lumpur, Malaysia.

Khier, W., Breur, M. and Durst, F. (2000), "Flow structure around trains under side wind conditions: a numerical study", *Comput. Fluids*, **29**(2), 179-195.

Krajnovic, S. and Davidson, L. (2004), "Large eddy simulation of the flow around an Ahmed body", *Proceedings of the ASME Heat Transfer/Fluids Engineering Summer Conference*, Charlotte, NC, USA.

Krajnovic, S., Ringqvist, P., Nakade, K. and Basara, B. (2012), "Large eddy simulation of the flow around a simplified train moving through a crosswind flow", *J. Wind Eng. Ind. Aerod.*, **110**, 86-99.

Menter, F.M. (1994), "Two-equation eddy-viscosity turbulence models for engineering application", *AIAA J.*, **32**(8), 1598-1605.

Orellano, A. and Schober, M. (2006), "Aerodynamic performance of a typical high-speed train", *Proceedings of the 4th WSEAS International Conference on Fluid Mechanics and Aerodynamics*, Elounda, Greece.

Osth, J. and Krajnovic, S. (2012), "Simulations of flow around a simplified train model with a drag reducing device using partially averaged navier-stokes", *Proceedings of the Conference on Modelling Fluid Flow (CMFF'12). The 15th International Conference on Fluid Flow Technologies,* Budapest, Hungary.

Per-Ake, T. (1999), "Experimentell undersökning av sidvindskänsligheten hos en model av en tvavaningsbuss I FFA:s vindtunnel LT1", *Report (in Swedish) FFA TN 2000-05*.

Prime, Z., Moreau, D., Doolan, C.J. and Mat Ali, M.S. (2014), "Flow modelling and noise generation of interacting prisms", *Proceedings of the 20th AIAA/CEAS Aeroacoustics Conference, Atlanta, GA.*

Rezvani, M.A. and Mohebbi, M. (2014), "Numerical calculations of aerodynamic performance for ATM train at crosswind conditions", *Wind Struct.*, **18**(5), 529-548.

Richardson, L.F. and Gaunt, J.A. (1927), "The deferred approach to the limit. Part I. Single Lattice. Part II. Interpenetrating lattices", *Philos. T. Roy. Soc. London. Series A, Containing Papers of a Mathematical or Physical Character*, **226**, 299-361.

Roache, P.J. (1994), "Perspective: A method for uniform reporting of grid refinement studies", *J. Fluid. Eng. -T ASME*, **116**(3), 405-413.

Robertson, E., Choudhury, V., Bhushan, S. and Walters D.K. (2015), "Validation of OpenFOAM numerical methods and turbulence models for incompressible bluff body flows", *Comput. Fluids,* **123**, 122-145.

Sakuma, Y. and Ido, A. (2009), "Wind tunnel experiments on reducing separated flow region around front ends of vehicles on meter-gauge railway lines", *Aerodynamic Laboratory, Environmental Engineering Division*, Japan **50**, 20-25.

Stern, F., Wilson, R.V., Coleman, H.W. and Paterson, E.G. (2001), "Comprehensive approach to verification and validation of CFD simulations part 1: Methodology and procedures", *J. Fluid. Eng. -T ASME*, **123**(4), 793-802.

Wilcox, D.C. (1993), "Comparison of two-equation turbulence models for boundary layers with pressure gradient", *AIAA J.*, **31**(8), 1414-1421.

Wilcox, D.C. (2006), Turbulence modelling for CFD, 3rd Ed., DCW Industries, Inc.

AD